Research Article Vol. 13, No. 8 / August 2026 / Optica 1649

# Reaching the intrinsic performance limits of superconducting nanowire single-photon detectors up to 0.1 mm wide

Kristen M. Parzuchowski,[1,2,†,*] Eli Mueller,[1,3,†] Bakhrom G. Oripov,[1,2] Benedikt Hampel,[1,2] Ravin A. Chowdhury,[1,2] Sahil R. Patel,[4,5] Daniel Kuznesof,[6] Emma K. Batson,[1,7] Ryan Morgenstern,[1,2] Robert H. Hadfield,[6] Varun B. Verma,[1] Matthew D. Shaw,[5] Jason P. Allmaras,[5] Martin J. Stevens,[1] Alex Gurevich,[8] and Adam N. McCaughan[1,2]

[1]Physical Measurement Laboratory, National Institute of Standards and Technology, 325 Broadway, Boulder, Colorado 80305, USA
[2]Department of Physics, University of Colorado, 2000 Colorado Avenue, Boulder, Colorado 80309, USA
[3]Department of Electrical Engineering, University of Colorado, 1200 Larimer Street, Denver, Colorado 80204, USA
[4]Department of Applied Physics and Materials Science, California Institute of Technology, 1200 E. California Boulevard, Pasadena, California 91125, USA
[5]Jet Propulsion Laboratory, California Institute of Technology, 4800 Oak Grove Drive, Pasadena, California 91109, USA
[6]James Watt School of Engineering, University of Glasgow, University Avenue, Glasgow G12 8QQ, Scotland, UK
[7]Department of Electrical Engineering and Computer Science, Massachusetts Institute of Technology, 77 Massachusetts Avenue, Cambridge, Massachusetts 02139, USA
[8]Department of Physics, Old Dominion University, 5155 Hampton Boulevard, Norfolk, Virginia 23529, USA
[†]These authors contributed equally to this work.
*kristen.parzuchowski@nist.gov

Received 10 April 2026; revised 23 July 2026; accepted 27 July 2026; published 19 August 2026

**Superconducting nanowire single-photon detectors combine high detection efficiency, low noise, and excellent timing resolution, making them a leading platform for photon-counting applications. However, despite decades of materials and fabrication research, detector performance has never been shown to match theoretical performance expectations. Here, we demonstrate *in situ* tuning of a detector from its typical, suboptimal operation, to a regime limited only by material quality, allowing the device to reach its intrinsic performance limit. Our approach is based on current-biased superconducting "rails" placed on either side of the detector that redistribute current across its width to achieve peak performance. This technique reduces the dark count rate by 10 orders of magnitude. Further, we show operation at this intrinsic performance limit for devices up to 0.1 mm wide and also demonstrate near-unity internal detection efficiency at a wavelength of 4 μm for a 20 μm wide detector—a factor of 20 wider than the current state of the art. This work enables future detectors to overcome the Pearl limit for device width, paving the way for arbitrarily large detectors.**

Published by Optica Publishing Group under the terms of the Creative Commons Attribution 4.0 License. Further distribution of this work must maintain attribution to the author(s) and the published article's title, journal citation, and DOI.

https://doi.org/10.1364/OPTICA.599984

## 1. INTRODUCTION

Single-photon detection underpins a wide range of emerging photonic technologies, from quantum information processing [1,2] and secure communications [3,4] to photon-starved biomedical imaging [5,6]. Among the available single-photon detector technologies, superconducting nanowire single-photon detectors (SNSPDs) are highly sought after for these applications, offering detection efficiencies exceeding 98% [7–9], dark count rates under 1 cnt/day [10], timing jitter below 3 ps [11], wire widths up to 60 μm [12–14], and sensitivity extending into the mid-infrared [15–17]. While these metrics are remarkable, they have each been optimized in isolation, with device designs tailored to enhance individual performance metrics at the expense of others. Numerous efforts to improve all-around device performance have focused on identifying promising superconducting films and then refining the fabrication protocols specific to each film. This time-consuming process has yielded real progress; however, it is generally incremental relative to theoretical performance expectations [18]. A central, but often overlooked reason for this performance gap is the limited operating current of the detector.

Among nominally identical SNSPDs, the highest performing devices are those that can be operated at the highest bias current. Although the theoretical upper bound on the total supercurrent is set by the depairing current $I_d$ [19], real devices transition to the resistive state at a reduced current known as the switching current

$I_{sw}$. Even in state-of-the-art SNSPDs, the ratio $I_{sw}/I_d$, sometimes called the constriction factor, rarely exceeds 0.7 [20–22].

The primary source of low $I_{sw}/I_d$ ratios is generally considered to be current pileup at the device edges. Current crowding lowers the energy barrier for vortex entry at the device boundaries and consequently increases the dark count rate. While current crowding in SNSPDs is often associated with sharp bends or corners in meander structures [23], a simple straight superconducting wire also exhibits a nonuniform current distribution across its width, with current density lowest in the middle and peaked near the edges. The mechanism of this edge current crowding is two-fold: First, real devices inevitably have lithographic defects along the edge of the wire, which lead to geometrical current crowding. Second, the Meissner effect causes a non-uniform flow of sheet current density $J(x)$ across the wire width, with $J(x)$ being lowest at the center and maximum at the edges. This current non-uniformity increases with the width of the wire $w$ [22] and is generally seen as the fundamental barrier that prevents the development of SNSPDs with wire widths approaching the scale of the magnetic Pearl length $\Lambda$ [24], typically on the order of 100's of μm in thin-film SNSPD materials [22,25]. Numerous strategies aimed at reducing the contribution of current crowding have been implemented [13,14,26,27], yielding significant performance gains over the years. However, never has there been a clear indicator that the detectors have reached their intrinsic limit, characterized by the onset of dark counts due to unbinding of vortex–antivortex (VAV) pairs [28]. For a given material, this limit is fundamental—it depends only on temperature and superconducting properties of the superconducting film.

Operating at currents far below $I_d$ can be detrimental to photon detection, especially at low photon energies. As the operating current is reduced, higher photon energies are necessary to reach the threshold to form a critical hotspot across the wire width. Because this threshold energy scales with the cross-sectional area of the detector, wide SNSPDs are typically inefficient for infrared detection. However, theoretical models predict that as $I_{sw}$ approaches $I_d$, the minimum detectable photon energy becomes only weakly dependent on wire width [18], allowing the possibility to develop SNSPDs with high efficiency into the infrared and ultra-wide widths surpassing the Pearl length. Here, we refer to these detectors as wide SNSPDs, retaining the widely recognized acronym. Although these detectors employ micrometer-scale rather than nanometer-scale widths, the acronym is used to ensure broad understanding of the detector type and its functionality. Scaling up the size of SNSPDs simplifies fabrication, enables higher signal amplitudes, unlocks polarization-insensitivity, and facilitates efficient free-space coupling.

In this work, we introduce a method to *in situ* tune $I_{sw}$ closer to $I_d$, thereby enabling the device to operate at its intrinsic performance limit. Our method relies on placing an SNSPD between two current-carrying superconducting "rails," as shown in Fig. 1(a). Here, the magnetic self-field of the rails partly cancels the perpendicular component of the self-field of the SNSPD, reducing the current density $J(x)$ at the edges [29,30]. This reduction inverts the typical $J(x)$ profile of a superconducting wire, yielding minima at the edges and a maximum at the center, thereby increasing the energy barrier for vortex entry from the edge of the wire. Figure 1(b) shows the evolution of $J(x)$ calculated by solving the London equation for different rail currents $I_r$ (see Supplement 1). The SNSPD-rail architecture not only eliminates the edge current crowding relative to that of a bare SNSPD without rails, but also allows *in situ* tuning of $J(x)$ at the edge by varying $I_r$ to reach the maximum performance. For instance, Fig. S2 in Supplement 1 shows tunable $J(x)$ profiles calculated for a 3 nm thick and 2.5 mm wide WSi wire that is 4 times larger than the Pearl length.

To measure the efficacy of this technique, we measured a variety of SNSPD-rail devices composed of thin-film WSi ($\Lambda = 600 \pm 30$ μm) SNSPDs with adjacent Nb rails. By turning on the rails, we demonstrate a 100 μm wide SNSPD with an over 10 orders-of-magnitude reduction in dark counts and a detection plateau at 1550 nm widened by more than 40%. In 20 μm wide SNSPDs, we reached near-unity internal detection efficiency (IDE) of 4 μm photons and lowered detector jitter by ≈ 30%. Furthermore, the rails allowed us to recover a detection plateau at 1550 nm in a device that would otherwise not be photosensitive because of its low $I_{sw}/I_d$ ratio. These significant improvements were made without compromising the photon detection efficiency across the width of the SNSPD. Our results show that the rails tune the device performance from an edge-limited to a material-limited dark count state. To our knowledge, this is the first demonstration of *in situ* tuning of an SNSPD to its intrinsic performance limit and establishes a pathway to scaling high-performing SNSPDs to widths exceeding the Pearl length.

## 2. RESULTS

Our SNSPD-rail architecture is illustrated in Fig. 1(a). An SEM image of a fabricated 50 μm wide WSi SNSPD with 4 μm wide adjacent Nb rails is shown in Fig. 1(c). Here, the ≈ 50 nm thick rails are displaced ≈ 150 nm from the edge of the SNSPD. The ≈ 3 nm thick WSi wire has a constriction length of 100 μm. We fabricated (see details in Methods) and tested numerous devices varying in SNSPD width from 1 to 100 μm. Device constriction length varied from 10 to 300 μm, which is mentioned only for clarity as length does not play a significant role in the results or analysis that follows. Here, we present representative experimental results from these devices. Unless otherwise specified, all measurements were performed in a fiber-coupled cryostat at $T = 900$ mK. The device chip was enclosed in an aluminum box at the low-temperature stage to minimize blackbody background. The output of the optical fiber (SMF-28) was coupled through a fiber port mounted on the aluminum box and was offset from the device chip by about 5 cm, thus producing flood illumination over the entire 1 $cm^2$ chip. For detector pulse readout, we used a wide-band bias tee (Mini-Circuits ZFBT-4R2GW-FT+) and two low-noise amplifiers (Mini-Circuits ZFL-1000LN+ and ZX60-P103LN+).

### A. Suppression of Dark Counts

Figure 1(d) shows the dark count rate as a function of the SNSPD bias current $I_s$ for a series of $I_r$ values for a 50 μm wide wire. The dark count rate follows a log-linear dependence on $I_s$, consistent with dark counts initiated by Arrhenius thermally activated vortex crossings [31] as described in Supplement 1. Increasing $I_r$ from 0 mA up to 11.8 mA shifts the dark count rate curve to higher $I_s$ values. For $I_r > 11.8$ mA (not shown), this trend reverses and the curve shifts to lower $I_s$. Here, $I_r^* \approx 11.8$ mA represents the optimal rail current that maximizes $I_{sw}$ of the SNSPD, where $I_{sw}$ is defined operationally as the value of $I_s$ at which the dark count rate exceeds 100 $s^{-1}$. The integration time for this measurement was 1 s, which limits the minimum measurable dark count rate

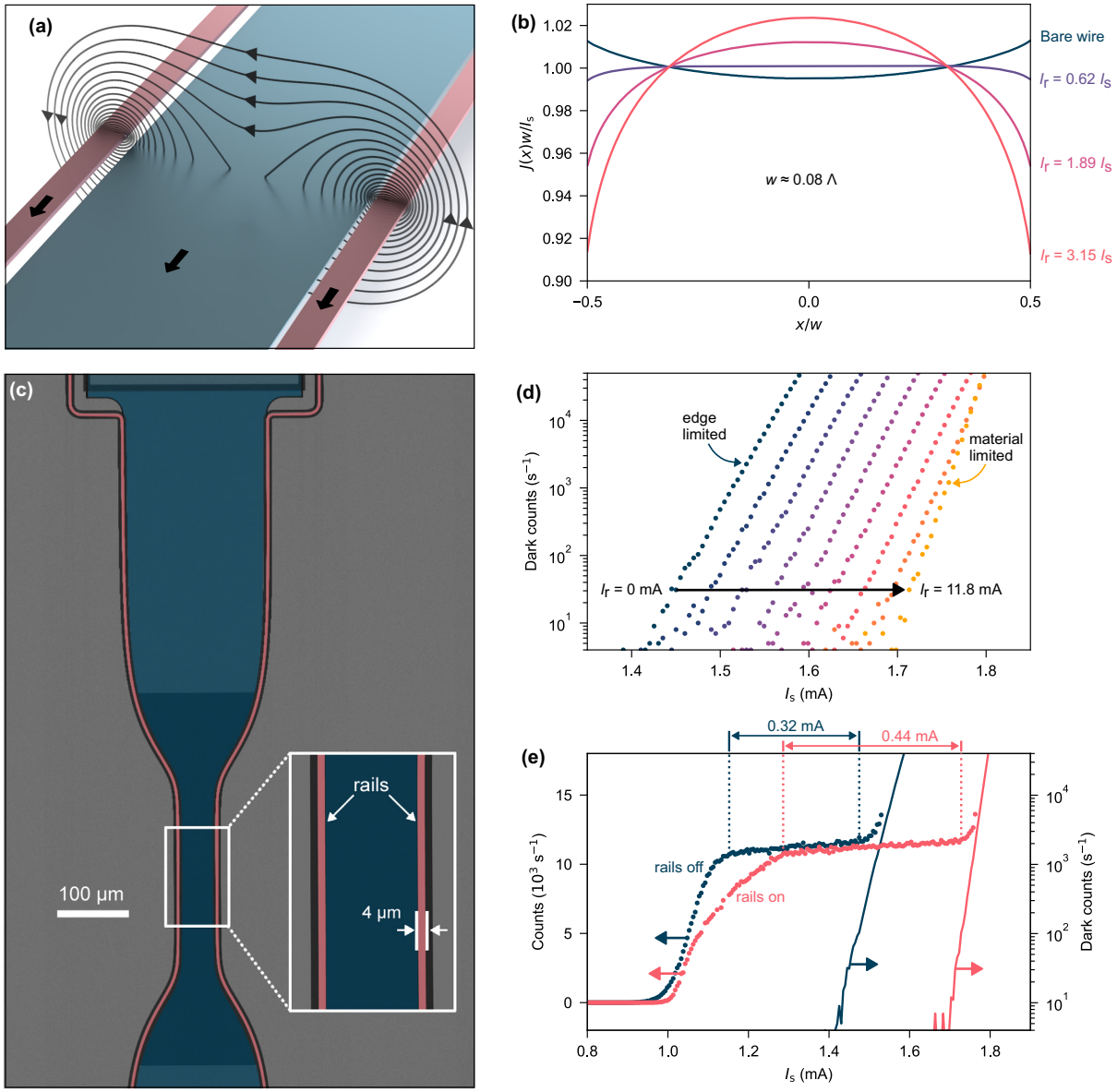


**Fig. 1.** (a) Illustration of an SNSPD (blue) integrated with adjacent rails (pink). Simulated magnetic field lines illustrate how the rails modify the self-induced magnetic field of the SNSPD. (b) Normalized current density as a function of position $x$ along the wire width $w$ simulated for a bare wire without rails (dark blue) and for a wire tuned by a series of increasing rail currents (purple to pink). For these simulations, the wire width is $w = 0.08\Lambda$ and the rails of width $0.15w$ are displaced from the edges of the wire horizontally and vertically by $w/200$. (c) False-color SEM image of 50 μm wide WSi wire (dark blue) with 4 μm wide Nb rails (pink). The WSi in the wide regions of the taper (lighter blue) is covered with an isolated layer of Nb. The inset shows a zoomed-in image of the constriction. (d) Measured dark count rate as a function of $I_s$ for a 50 μm wide wire for a series of increasing $I_r$ values from 0 mA (dark blue) to 11.8 mA (yellow). Dark counts onset at higher $I_s$ as $I_r$ is increased. The blackbody background in this measurement was below approximately 4 $s^{-1}$, which corresponds to the lower limit of the $y$ axis and is therefore not visible in the plot. (e) Measured flood-illuminated 1550 nm photon count rate (left vertical axis, data points) and dark count rate (right vertical log-scale axis, lines) as a function of $I_s$ for rails off (dark blue) and on (pink) for a 50 μm wide wire. Gold covers were placed over the tapers of the SNSPD to prevent detection events outside the constriction. The plateau width is ≈320 μA with rails turned off and extends to ≈440 μA with rails turned on. The start of the plateau was set as the value of $I_s$ at which the count rate exceeds $10.7 \times 10^3$ $s^{-1}$. The end of the plateau was set as the value at which the dark count rate exceeds 100 $s^{-1}$.

to 1 $s^{-1}$. We extrapolated the $I_r^*$ dark count curve to the $I_s$ value at which the dark counts are 1000 $s^{-1}$ for $I_r = 0$ and estimate a more than 9 orders-of-magnitude reduction in dark counts at $I_r^*$ relative to $I_r = 0$. At $I_r \approx I_r^*$, there is an abrupt increase in the slope of the dark count rate curve that persists for $I_r > I_r^*$. As will be discussed below, this slope increase is indicative of a transition from a regime where dark counts are dominated by penetration of vortices from the edges ($I_r < I_r^*$), to a regime where dark counts are dominated by unbinding of VAV pairs in the bulk material ($I_r \geq I_r^*$). Here, the intrinsic performance limit has been reached when $I_r = I_r^*$, and further increases in $I_r$ result in a gradual loss of peak performance due to an increasingly nonuniform current density. Note that reversing the rail current polarity such that $I_s$ and $I_r$ flow in opposite directions shifts the dark count rate curve to lower $I_s$ values, thereby degrading device performance.

### B. Impact on Photosensitivity

Figure 1(e) shows the count rate as a function of $I_s$ for the same 50 μm wide device under flood illumination of $\lambda = 1550$ nm light with the rails off ($I_r = 0$ mA) and with the rails on ($I_r = I_r^*$). The count rate reaches a detection plateau, indicating saturated IDE, both with the rails on and off. Note that with the rails on, the onset of photosensitivity shifts to higher $I_s$ values compared to that with the rails off; however, the dark-count onset shifts by an even larger amount, resulting in a ≈ 40% increase in the detection plateau length. We also observed that the photosensitivity onset with the rails on deviates from a typical sigmoid shape. We review both of these photosensitivity-onset features in Section 3.

Similarly, Fig. 2(a) shows the count rate as a function of $I_s$ for a 100 μm wide device with 10 μm constriction length under flood illumination of $\lambda = 1550$ nm light with the rails off ($I_r = 0$ mA) and with the rails on ($I_r = I_r^* \approx 11.1$ mA). For this measurement, the pulse amplitude was so large that amplifiers were not used. The count rate exhibits a slope on the plateau that we attribute to photon detection events in the taper of the device. In contrast, the plateau in Fig. 1(e) is flat, as the tapers in that device were blocked with a gold layer. Similar to Fig. 1(e), turning the rails on shifts the onset of photosensitivity to higher $I_s$ values, while the dark-count onset shifts by a larger amount, resulting in a ≈ 44% increase in the detection plateau length. We extrapolated the $I_r^*$ dark count curve to the $I_s$ value at which the dark counts are 1000 $s^{-1}$ for $I_r = 0$ and estimate a more than 10 orders-of-magnitude reduction in dark counts at $I_r^*$ relative to $I_r = 0$.

To test the upper bound on the wavelength sensitivity of our SNSPD-rail devices, we tested a 20 μm wide SNSPD with 300 μm constriction length in a ≈ 260 mK cryostat [16] fit with an optical window for free-space coupled infrared light sources, which in this case was a blackbody source with a temperature of 630 K, and a monochromator at the 40 K stage used for precise wavelength selection. This optical window resulted in higher background photon counts than the fiber-coupled experiments at 1550 nm [Figs. 1(d) and 2(a)]. Figure 2(b) shows the background-subtracted photon count rate of the 20 μm wide SNSPD under flood illumination of $\lambda = 4$ μm photons as a function of $I_s$ with the rails off ($I_r = 0$ mA) and with the rails on ($I_r = I_r^* \approx 10.1$ mA). The background counts due to this light source and cryostat are evident in the $I_s = 550$ μA−675 μA range before the log-linear dark counts dominate. By turning on the rails, the dark counts are reduced enabling measurement of the 20 μm wide wire's photon count rate at higher $I_s$. The count rate at higher $I_s$ increases and rolls over onto the start of a detection plateau, indicating near-unity IDE. This result represents a factor of 20 increase in wire width compared to the current state of the art for high-efficiency SNSPDs at mid-infrared wavelengths [17]. We note that during this measurement, biasing the rails at $I_r^*$ increased the operating temperature by approximately 120 mK due to Joule heating, likely due to the high-resistivity CuNi coaxial cabling at the low-temperature stage. This heating could be mitigated by instead using superconducting coaxial cables.

To determine if the rails could recover an otherwise non-functional detector, we also tested several devices that showed unusually low $I_{sw}/I_d$ ratios. We attribute the poor performance of these outlier devices to severe lithographic defects [32], which are inevitably present in a small fraction of devices in any lithographic process. In Fig. 3, the measured flood-illuminated 1550 nm photon count rate and dark count rate are plotted as a function of $I_s$ for one of these devices. This device is 10 μm wide with a 300 μm constriction length. With the rails off ($I_r = 0$ mA), $I_{sw}/I_d \approx 44\%$ and the dark counts dominate at such a low $I_s$ values that the wire has no photosensitivity to 1550 nm photons. With the rails on ($I_r = 20.9$ mA), the dark count curve shifts dramatically to higher $I_s$ values, reaching $I_{sw}/I_d \approx 63\%$, and photon counts can be measured with near-unity IDE. Thus, the rails recovered the performance of the SNSPD that otherwise would have been non-functional at 1550 nm.

### C. Impact on Timing Jitter

Figure 4(a) shows the histogram of detection latency for a 20 μm wide wire with 300 μm constriction length under 1550 nm flood illumination for six $I_r$ values ranging from $I_r = 0$ to $I_r = 8.8$ mA. The long tail is likely due to detection events in the taper of our wires as has been noted in previous studies [11]. As $I_r$ is increased,

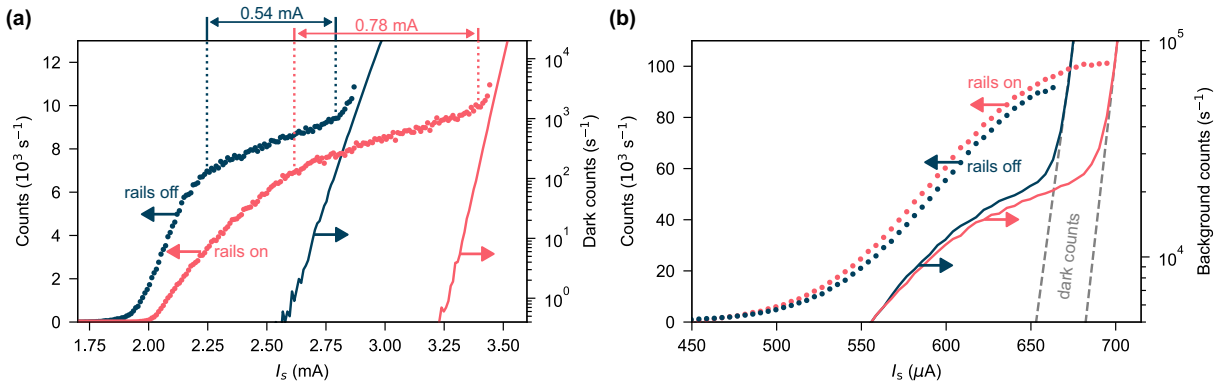


**Fig. 2.** (a) Measured flood-illuminated 1550 nm photon count rate (left vertical axis, data points) or dark count rate (right vertical log-scale axis, lines) as a function of $I_s$ for rails off (dark blue) or rails on (pink) for a 100 μm wide wire. The plateau width is ≈ 540 μA with rails turned off and extends to ≈ 780 μA with rails turned on. The start of the plateau was set as the value of $I_s$ at which the count rate exceeds $6.9 \times 10^3$ $s^{-1}$. The end of the plateau was set as the value at which the dark count rate exceeds 100 $s^{-1}$. (b) Measured background-subtracted, flood-illuminated 4 μm photon count rate (left vertical axis, data points) and background count rate (right vertical log-scale axis, lines) for a 20 μm wide wire as a function of $I_s$ for rails off (dark blue) and rails on (pink). At low $I_s$, the background counts are dominated by blackbody background photons entering through the optical window on the cryostat, then, as $I_s$ is increased, the exponential dark counts takeover as indicated by the dashed gray line. Turning on the rails shifts the dark counts to higher $I_s$ values, enabling measurements at higher $I_s$ values. In this region, a rollover of counts is observed, indicating the start of a plateau and near-unity IDE.

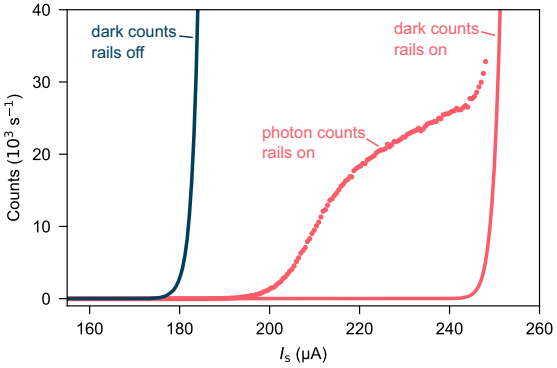


**Fig. 3.** Measured flood-illuminated 1550 nm photon count rate (pink data points) and dark count rate (lines) as a function of $I_s$ for rails off (dark blue) and rails on (pink) for a 10 μm wide wire with a low $I_{sw}/I_d$ ratio. With the rails off, the dark counts begin to dominate at such a low $I_s$ that photon counts cannot be measured. With the rails on, a huge shift of dark counts to higher $I_s$ is observed, and photon counts are measured with near-unity IDE. The slope on the plateau is consistent with photon detection events in the taper of the device.

the histogram narrows. We suspect that this may be caused by the merging of two latency distributions: one originating from edge vortex-mediated detections and another from VAV-pair-mediated detections; however, a more thorough study is necessary to confirm this hypothesis.

In Fig. 4(b), the full width at half-maximum (FWHM) system jitter is plotted as a function of $I_r$ for several devices with 300 μm constriction lengths and widths of 5, 10, and 20 μm. There is no clear dependence of jitter on wire width; however, all wires demonstrate improved jitter upon application of rail current until an optimum value is reached. This optimum jitter value typically occurred at an $I_r$ value that differed from $I_r^*$ by a few milliamperes. After this optimum jitter value, the jitter slightly increases as the rail current is increased further. Interestingly, the optimum jitter of all three wire widths is similar, ≈ 35 ps.

We measured several contributions to the system jitter, including the time tagger single-channel jitter, the laser sync jitter, the sync-to-optical jitter, and the laser period jitter, which have FWHM contributions of 13.6, 5.6, 2.1, and ≈ 3.4 ps, respectively. The remaining contributions are from the noise jitter of the SNSPD pulse [33], the intrinsic variations in the generation of a hotspot, and the geometric jitter of the SNSPD. We estimate the standard deviation of the longitudinal geometric jitter to be 10.0, 7.9, and 6.3 ps for the 5, 10, and 20 μm wide devices, respectively. Further study is required to fully quantify the total geometric jitter.

### D. Tunable Proximity to the Depairing Current

As a demonstration of how the rails impact the switching current, Fig. 5 shows $I_{sw}/I_d$ as a function of $I_r$ for a 20 μm wide device with 100 μm constriction length, a 50 μm wide device with 100 μm constriction length, and a 100 μm wide device with 10 μm constriction length. Here, $I_{sw}$ is defined as the value of $I_s$ at which the dark count rate exceeds 100 $s^{-1}$. For all wire widths, $I_{sw}/I_d$ increases for positive $I_r$ and reaches a peak over the range of $I_r$ measured. This peak occurs at $I_r^*$. Although the 20 μm wire data were not measured past the peak, it was confirmed that the maximum $I_r$ value tested corresponded to the point at which the slope of the dark count rate versus $I_s$ curve steepened, suggesting the device has reached its performance limit. As wire width increases, the change in $I_{sw}/I_d$ with $I_r$ becomes more significant. This trend is consistent with our calculations that show that wider wires with correspondingly stronger edge current crowding benefit more from its suppression by the rails.

To determine the depairing current of our film, which was used in Fig. 5, we measured the change in kinetic inductance of step-impedance resonators as a function of bias current as described in Ref. [20]. These resonators were fabricated from a nominally identical film to that used for the SNSPD-rail devices. The measured kinetic inductance change was fit to the fast and slow relaxation models described in Ref. [34]. We found that the fast relaxation model was a better fit for all resonators. These fits were used to derive the depairing current per unit of wire width with an average of 39 μA $μm^{-1}$.

## 3. DISCUSSION

Our results show that SNSPD-rail devices reverse current crowding at the wire edges and remove the fundamental Pearl length limitation on wire width. This also follows from our numerical calculations that show that the current density at the edges can be reduced lower than that in the center of the wire even for an SNSPD with $w \gg \Lambda$. Moreover, the required reduction of $J(x)$ at the edges is achieved with a normalized rail current $I_r/I_s$ that diminishes as the wire width increases from $w \ll \Lambda$ to $w > \Lambda$. Although some superconducting devices suffer consequences from the linear increase in magnetic flux trapping with device area, here

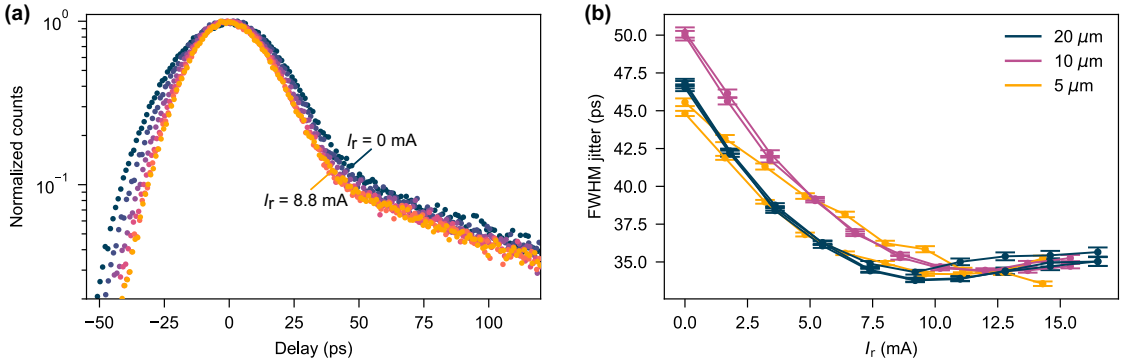


**Fig. 4.** (a) Jitter histograms for a 20 μm wide wire under 1550 nm flood illumination for six $I_r$ values ranging from $I_r = 0$ to $I_r = 8.8$ mA. The long tail onsetting at ≈ 40 ps delay time is likely due to detection events in the taper. The jitter histogram narrows as $I_r$ is increased. (b) The FWHM system jitter as a function of $I_r$ for two 5 μm (yellow), two 10 μm (pink), and three 20 μm (dark blue) wide wires. As $I_r$ is increased, the jitter decreases until it reaches a minimum.

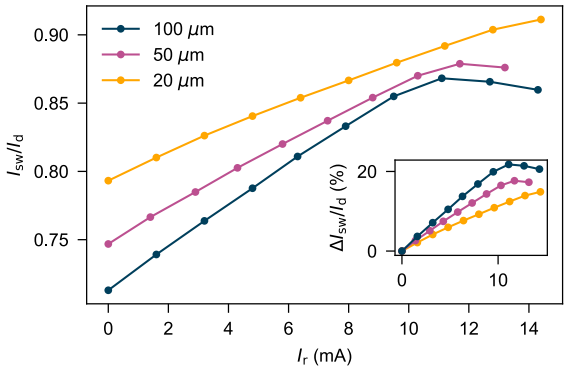


**Fig. 5.** Measured $I_{sw}/I_d$ as a function of $I_r$ for wire widths of 20 μm (yellow), 50 μm (pink), and 100 μm (dark blue). As $I_r$ is increased, $I_{sw}/I_d$ also increases until it reaches $I_r^*$. Percent change (Δ) in $I_{sw}/I_d$ as a function of $I_r$ is shown in the inset for the same devices. As wire width is increased, larger increases in $I_{sw}/I_d$ are measured.

the direct current flowing through the SNSPD flushes out the flux trapped during the cooldown, yielding no consequences. We anticipate that the next limitation to scale to wider SNSPD widths may be set by a degradation in film quality over large length scales.

We observed that for all devices, $I_{sw}(w)$ are maximized at optimum rail currents $I_r^*(w)$. The slopes of the log-linear dark count rates as a function of $I_s$ (such as that shown in Fig. 1(d)) increase abruptly at $I_r = I_r^*$. The dark count rate $S$ generally follows a thermally activated Arrhenius behavior caused by penetration of vortices from the edge given by $S_e(I_s) \simeq S_{e0} \times \exp[-(1 - I_s/I_d)U_e/T]$, where $U_e$ is the energy barrier for vortex entry. For the data $I_r < I_r^*$, we have $U_e \approx 83$ K for the 50 μm wide wire shown in Fig. 1(d) and $U_e \approx 71$ K for the 100 μm wide wire shown in Fig. 2(a). These values of $U_e$ are consistent with our evaluation of the vortex energy barrier for penetration of vortices from the edges given in Supplement 1. In turn, the nearly doubling of the logarithmic slope observed at $I_r > I_r^*$ is strong experimental evidence that the dark count rate becomes dominated by the unbinding of VAV pairs of radius $\sim \xi J_d/J \ll w$ in the center of the wire. This is because the energy of a vortex spaced by $u$ from an ideal edge of a wire is half the energy of a VAV pair of radius $u$ in the bulk of a wire, so that now the dark count rate is given by $S_b(I) \simeq S_{b0} \exp[-(1 - I_s/I_d)U_b/T]$, where $U_b = 2U_e$.

As shown in Supplement 1, the ratio of the logarithmic slopes $\partial_{I_s} \ln S$ for vortex hopping from the edges and for VAV pair production are related by $\partial_{I_s} \ln S_b / \partial_{I_s} \ln S_e \simeq 2\tilde{J}_d/J_d$, where $J_d$ and $\tilde{J}_d$ are the mean depairing current densities in the bulk and at the edges, respectively. Here, $\tilde{J}_d$ is reduced relative to $J_d$ by the current crowding at lithographic defects. For instance, the slope ratio $\approx 1.79$ observed in the 50 μm wide wire shown in Fig. 1(d) implies $\tilde{J}_d = 0.895\, J_d$ and the ratio $\approx 1.53$ observed in the 100 μm wide wire shown in Fig. 2(a) implies $\tilde{J}_d = 0.765\, J_d$. To mitigate penetration of vortices from the edges for these wires, the rails should carry current sufficient to reduce $J(x)$ at the edges by 10.5% and 23.5%, respectively.

Two important conclusions follow from our analysis of dark counts: (1) In addition to increasing $I_{sw}$, the rails greatly (up to 10 orders of magnitude) reduce dark counts caused by penetration of vortices from the edges. (2) At $I_r = I_r^*$, the wire achieves its maximum $I_{sw}/I_d$. As stated above, we define $I_{sw}$ as the current at which the dark count rate equals 100 $s^{-1}$. The VAV pair unbinding makes it impossible to reach $I_s = I_d$ in a wire without switching to the resistive state, but the rails do allow the device to operate at its intrinsic performance limit with maximum photon sensitivity. In addition to the fundamental limits of $I_{sw}$ and the SNSPD sensitivity, which are both caused by the VAV pair production evaluated in Supplement 1, there are also technological and materials science limitations to its maximum value. These limitations result from variations in film thickness, lithographic defects, inhomogeneities of superconducting properties due to local non-stoichiometry, grain boundaries in polycrystalline films, film adhesion with the substrate, etc. Beyond these limitations, our estimated $I_d$ has uncertainty associated with it. For example, our method for estimating $I_d$ of our devices uses assumptions from the BCS model that do not account for the effects of strong electron–phonon pairing of the Eliashberg theory [35], or the reduction of $J_d$ by subgap quasiparticle states [36], both of which are especially pronounced in thin, superconducting films. Nonetheless, tuning $J(x)$ by rails enables reaching the intrinsic limit of $I_{sw}$ for a particular SNSPD even if both the exact value of $J_d$ and the extent of reduction of $J_d$ at the edges are unknown.

We observed that current redistribution in SNSPDs was possible without affecting detection efficiency uniformity; the photon count rate on the detection plateau varies by less than 1% across the full range of $I_r$ as described in the Methods section. However, the results shown in Figs. 1(e) and 2(a) clearly show that the onset of photosensitivity shifts slightly to higher $I_s$ values with the rails on. This behavior may reflect a nonuniform threshold current density for photodetection across the wire in which the photon detections near the edge have a lower detection threshold current density than that in the bulk [37–39]. In this scenario, when the rails are turned off, the edges will become photosensitive at lower $I_s$ values relative to that for the bulk. However, when the rails are turned on and the current density near the edges is reduced, a higher total $I_s$ is required for the edge to reach its threshold current density, shifting the onset of photosensitivity to higher $I_s$ values. We also observed a change in shape of the photosensitivity-onset curve with the rails turned on for the measurements at $T \approx 0.9$ K under $\lambda = 1550$ nm illumination [Figs. 1(e), 2(a)], which may also be a result of the reduced current density at the edges of the wire. Notably, this effect, which broadens the onset and causes a deviation from a typical sigmoidal curve, was not observed for the measurements at $T \approx 260$ mK under $\lambda = 4$ μm illumination [Fig. 2(b)]. This suggests that the effect is strongly dependent on photon energy and/or thermal fluctuations as has been reported previously [40–42]. However, several mechanisms are known to influence the functional form of the IDE as a function of $I_s$ [43], and distinguishing among the possible mechanisms is beyond the scope of this work.

Turning to the timing jitter observed in our devices, the ≈ 50 ps jitter on our devices up to 20 μm wide warrants further discussion. This result seems inconsistent with models in which components of the VAV pair generated by a photon near the edge and in the center of the wire have different transit times [18] so that wider wires would have greater timing jitter. This model, along with previous experiments studying jitter dependence on wire width [11], has primarily focused on nanowires ≈ 100 nm wide. It remains unclear how the jitter scales as the widths increase to 1 μm–100 μm. For instance, taking the terminal velocity of a vortex $v_c \simeq 20$ km $s^{-1}$ measured on Pb film bridges [44] at $J \approx J_d$, one would expect a geometric jitter of $\sim w/v_c \sim 1$ ns in a 20 μm wide wire, which is

20 times larger than the observed jitter of ∼50 ps shown in Fig. 4. The value of $v_c$ observed on Pb is qualitatively consistent with the estimate $v_c \simeq J_d/\eta \simeq \rho_n \xi/2\mu_0\lambda^2$, where $\eta = \phi_0^2/2\pi\xi^2\rho_n$ is the Bardeen–Stephen vortex drag coefficient, $\rho_n$ is a normal-state resistivity at $T_c$, and $J_d \simeq \phi_0/4\pi\mu_0\lambda^2\xi$. The same estimate of $v_c$ for our WSi film with $\xi = 10$ nm, $\lambda = 950$ nm, and $\rho_n = 2.5\ \mu\Omega$ m yields $v_c \sim \rho_n\xi/2\mu_0\lambda^2 \sim 11\ \mathrm{km\ s^{-1}}$, which again predicts a jitter substantially larger than that observed on the 20 μm wide SNSPD. Thus, real devices significantly outperform the estimates of conventional models of a vortex-assisted jitter, showing that our current understanding of the dynamics of a resistive domain produced by photon absorption is still incomplete.

It is worth noting that the ultra-wide SNSPDs studied here showed broad detection plateaus for 1550 nm photons even without applying rail current. In addition, a control device without rails, or otherwise any Nb nearby, also demonstrated a similar detection plateau, indicating that the rail structures are not always required for high-efficiency photosensitivity to 1550 nm photons. This result is remarkable, and we attribute this to several factors. First, our use of electron-beam lithography and the relatively short wire lengths in our devices help minimize edge defects [45], resulting in relatively high $I_{sw}/I_d$ compared to those noted in previous works [20–22]. Second, our detectors are made from a highly uniform amorphous superconductor [46] and the thin-film WSi recipe has a high silicon content (≈ 0.48Si mole fraction) designed to maximize photosensitivity in wide wires [21]. We also note that our wires do not self reset without shunting the device with an inductor and resistor in parallel with the SNSPD at low temperature. We used a PdAu shunt resistor that was nominally 1 Ω and a Nb spiral inductor that ranged from 0.2 to 1 μH depending on the experiment. This shunting requirement is likely generic to ultra-wide SNSPDs and may have caused wide wires to be overlooked in the past.

Other SNSPD designs have similarities to our SNSPD-rail architecture—superconducting nanowire avalanche detectors (SNAPs) [47,48] have multiple parallel adjacent wires that frequently employ parallel currents. However, the magnitude of the currents in neighboring wires are all equal, which will have a very small effect on the current distribution of the neighboring wires. As noted above, narrow central wires, like those typically used in SNAP, require higher normalized rail current $I_r/I_s$ to achieve the same effect as that for wide central wires. Another similar design is the meander-style SNSPD [49,50] that has multiple parallel adjacent wires flowing antiparallel currents. This design also uses equal current magnitudes and narrow wires, likely yielding no noticeable effect. We also note that the broader concept of engineering edge vortex barriers has previously been explored, for example by intentionally roughening one edge of a superconducting strip to produce asymmetric vortex entry and flux rectification under an applied dc magnetic field [51].

To our knowledge, the widest SNSPDs tested to date are 60 μm wide detectors made from approximately 2 nm thick MoSi films [12]. These devices demonstrated single-photon sensitivity at wavelengths up to 1550 nm, however they did not show saturated IDE. In two recent works by Yabuno *et al*. [13,14], SNSPDs of width 20 μm made from NbTiN thin films were demonstrated. In this study, the authors used a "high critical current bank (HCCB)" structure, in which the center of the wire material is irradiated with ions to selectively lower $I_d$ relative to the edges. For a fixed current flowing through the wire, this irradiation allows the center to operate closer to $I_d$ than without irradiation. This approach worked extremely well, demonstrating near-unity IDE at 2 μm for the 20 μm wide wire. However, the HCCB does not suppress the edge current crowding caused by Meissner screening, but instead partially compensates for it by reducing $I_d$ in the center relative to the edges. If the wire width continues to approach and exceed the Pearl length, the current crowding will become more pronounced and eventually exceed the additional vortex energy barrier provided by the HCCB. Therefore, the fundamental limitation on the maximum size of wire width achievable using this approach is still limited by the Pearl length.

Finally, in addition to boosting the performance limits of any given SNSPD, the rails can also help resolve the Berezinskii–Kosterlitz–Thouless (BKT) transition in thin films [28]. As pointed out above, the abrupt change in the slope of the dark count rate at the optimum rail current $I_r^*$ shown in Fig. 1(d) is a clear experimental indication of the suppression of single-vortex penetration from the edges and a transition to BKT unbinding of VAV pairs inside the film. Thus, using rails can be helpful in fundamental investigations of the BKT transition without the masking effects of edge-induced vortex entry.

## 4. CONCLUSION

We have demonstrated, for the first time, a method to *in situ* tune the performance of an SNSPD to its intrinsic limit, paving the way to scale to higher-performing detectors as well as wire widths exceeding the Pearl length. The approach uses current-biased superconducting rails on each side of the wire to reduce the current density at the edges, allowing the device to operate at a higher fraction of the depairing current. We pushed a 100 μm wide SNSPD to its intrinsic performance limit, demonstrating an extension of the detection plateau at 1550 nm and over 10 orders-of-magnitude reduction in dark counts. We demonstrated that rails provide numerous other follow-on performance benefits to SNSPD technology including increased upper bound of wavelength sensitivity, recovery of detector functionality in low-performing devices, and improved detector jitter.

The orders-of-magnitude reduction in dark counts has positive consequences for scaling these detectors into arrays. In an array, the total dark count rate is multiplied by the number of individual detectors and thus can quickly add up to a sizeable number of dark counts [52]. With rails, the dark counts can be easily reduced to a nearly negligible rate.

The ability to scale to wide wires is also important and previously was inaccessible. Wide wires eliminate the need to meander a detector to create a high fill factor [50]. With a focused or fiber-coupled beam, all of the photons of interest can be collected onto our 100 μm wide detector. Scaling these wide wires up into arrays, the fill factor can be much higher than previous demonstrations [52]. Furthermore, meandered detectors are sensitive to the polarization of light, with light polarized parallel to the straight sections of the detector being less efficiently detected. In contrast, our wide detectors consist of a single wire that can cover the entire focused beam spot, allowing maximum optical efficiency for all polarizations.

In future studies, we foresee being able to scale these detectors to widths wider than the Pearl length, which could yield high-efficiency free-space coupled SNSPDs—eliminating the need for lossy fiber optics. These detectors could be immediately applied to

quantum information experiments, where loss is detrimental to the fidelity of the transmitted quantum state [1,4].

**Funding.** National Institute of Standards and Technology; University of Colorado Boulder; University of Colorado Denver; National Academies of Sciences, Engineering, and Medicine; Defense Advanced Research Projects Agency; Engineering and Physical Sciences Research Council; Science Foundation Ireland.

**Acknowledgment.** D. Kuznesof thanks the EPSRC and SFI Centre for Doctoral Training in Photonic Integration for Advanced Data Storage (CDT-PIADS EP/S023321/1). Certain commercial equipment, instruments, or materials are identified in this paper in order to specify the experimental procedure adequately. Such identification is not intended to imply recommendation or endorsement by NIST nor is it intended to imply that the materials or equipment identified are necessarily the best available for the purpose.

**Disclosures.** The authors declare no conflicts of interest.

**Data availability.** Data underlying the results presented in this paper are not publicly available at this time but may be obtained from the authors upon reasonable request.

**Supplemental document.** See Supplement 1 for supporting content.

## REFERENCES

1. S. J. White, E. Polino, F. Ghafari, *et al.*, "Robust approach for time-bin-encoded photonic quantum information protocols," Phys. Rev. Lett. **134**, 180802 (2025).
2. N. Dalbec-Constant, G. Thekkadath, D. England, *et al.*, "Accurate unsupervised photon counting from transition-edge-sensor signals," Phys. Rev. Appl. **24**, 034018 (2025).
3. F. Grünenfelder, A. Boaron, G. V. Resta, *et al.*, "Fast single-photon detectors and real-time key distillation enable high secret-key-rate quantum key distribution systems," Nat. Photonics **17**, 422–426 (2023).
4. M. Jabir, R. B. Dawkins, J. Sabines-Chesterking, *et al.*, "Precision channel loss estimation for quantum networks," Optica **12**, 2001–2007 (2025).
5. Q. Wang, M. Pan, L. Kreiss, *et al.*, "A comprehensive overview of diffuse correlation spectroscopy: theoretical framework, recent advances in hardware, analysis, and applications," NeuroImage **298**, 120793 (2024).
6. E. C. V. Hughes, A. Upadhya, and K. Dholakia, "Superconducting nanowire single-photon detectors for enhanced biomedical imaging," J. Biomed. Opt. **31**, 113502 (2026).
7. D. V. Reddy, R. R. Nerem, S. W. Nam, *et al.*, "Superconducting nanowire single-photon detectors with 98% system detection efficiency at 1550 nm," Optica **7**, 1649–1653 (2020).
8. P. Hu, H. Li, L. You, *et al.*, "Detecting single infrared photons toward optimal system detection efficiency," Opt. Express **28**, 36884–36891 (2020).
9. J. Chang, J. Los, J. Tenorio-Pearl, *et al.*, "Detecting telecom single photons with 99.5 − 2.07 + 0.5% system detection efficiency and high time resolution," APL Photonics **6**, 036114 (2021).
10. J. Chiles, I. Charaev, R. Lasenby, *et al.*, "New constraints on dark photon dark matter with superconducting nanowire detectors in an optical haloscope," Phys. Rev. Lett. **128**, 231802 (2022).
11. B. Korzh, Q.-Y. Zhao, J. P. Allmaras, *et al.*, "Demonstration of sub-3 ps temporal resolution with a superconducting nanowire single-photon detector," Nat. Photonics **14**, 250–255 (2020).
12. X. Zhang, I. Charaev, H. Liu, *et al.*, "Physical properties of amorphous molybdenum silicide films for single-photon detectors," Supercond. Sci. Technol. **34**, 095003 (2021).
13. M. Yabuno, F. China, H. Terai, *et al.*, "Superconducting wide strip photon detector with high critical current bank structure," Opt. Quantum **1**, 26–34 (2023).
14. M. Yabuno, F. China, H. Terai, *et al.*, "Two-micron-wavelength single-photon detection using the high-critical-current-bank structure superconducting wide strip photon detector," Opt. Express **33**, 24927–24936 (2025).
15. G. G. Taylor, A. B. Walter, B. Korzh, *et al.*, "Low-noise single-photon counting superconducting nanowire detectors at infrared wavelengths up to 29 μm," Optica **10**, 1672–1678 (2023).
16. B. Hampel, D. Kuznesof, A. S. Mueller, *et al.*, "Tungsten germanide superconducting nanowire single-photon detectors with saturated internal detection efficiency at wavelengths up to 29 μm," APL Photonics **11** 066112 (2026).
17. Y.-Z. Wang, W.-J. Zhang, X.-Q. Zheng, *et al.*, "Saturated single-photon detection up to 5 μm in the mid-infrared using nbn superconducting microstrip detectors," Superconductivity **17**, 100232 (2026).
18. D. Y. Vodolazov, "Single-photon detection by a dirty current-carrying superconducting strip based on the kinetic-equation approach," Phys. Rev. Appl. **7**, 034014 (2017).
19. M. Tinkham, *Introduction to Superconductivity* (Courier Corporation, 2004).
20. S. Frasca, B. Korzh, M. Colangelo, *et al.*, "Determining the depairing current in superconducting nanowire single-photon detectors," Phys. Rev. B **100**, 054520 (2019).
21. J. Chiles, S. M. Buckley, A. Lita, *et al.*, "Superconducting microwire detectors based on WSi with single-photon sensitivity in the near-infrared," Appl. Phys. Lett. **116**, 242602 (2020).
22. T. Haneishi, M. Yabuno, H. Kutsuma, *et al.*, "Evaluation of NbTiN superconducting strip photon detectors with 0.1–30 μm strip widths," IEEE Trans. Appl. Supercond. **35**, 2200105 (2024).
23. J. R. Clem and K. K. Berggren, "Geometry-dependent critical currents in superconducting nanocircuits," Phys. Rev. B **84**, 174510 (2011).
24. J. Pearl, "Current distribution in superconducting films carrying quantized fluxoids," Appl. Phys. Lett. **5**, 65–66 (1964).
25. X. Zhang, A. Engel, Q. Wang, *et al.*, "Characteristics of superconducting tungsten silicide $W_xSi_{1-x}$ for single photon detection," Phys. Rev. B **94**, 174509 (2016).
26. R. Baghdadi, E. Schmidt, S. Jahani, *et al.*, "Enhancing the performance of superconducting nanowire-based detectors with high-filling factor by using variable thickness," Supercond. Sci. Technol. **34**, 035010 (2021).
27. S. Strohauer, F. Wietschorke, C. Schmid, *et al.*, "Current crowding–free superconducting nanowire single-photon detectors," Sci. Adv. **11**, eadt0502 (2025).
28. B. Halperin and D. R. Nelson, "Resistive transition in superconducting films," J. Low Temp. Phys. **36**, 599–616 (1979).
29. V. L. Newhouse, "Superconducting devices," in *Superconductivity*, R. D. Parks, ed. (Marcel Dekker, 1969), Vol. **2**, pp. 1283–1342.
30. L. R. Cadorim, E. Sardella, and C. C. S. Silva, "Harnessing the superconducting diode effect through inhomogeneous magnetic fields," Phys. Rev. Appl. **21**, 054040 (2024).
31. L. Bulaevskii, M. Graf, C. Batista, *et al.*, "Vortex-induced dissipation in narrow current-biased thin-film superconducting strips," Phys. Rev. B **83**, 144526 (2011).
32. A. Silhanek, L. Jiang, C. Xue, *et al.*, "Impact of border defects on the magnetic flux penetration in superconducting films," Appl. Phys. Rev. **12**, 041324 (2025).
33. M. Caloz, B. Korzh, E. Ramirez, *et al.*, "Intrinsically-limited timing jitter in molybdenum silicide superconducting nanowire single-photon detectors," J. Appl. Phys. **126**, 164501 (2019).
34. J. R. Clem and V. Kogan, "Kinetic impedance and depairing in thin and narrow superconducting films," Phys. Rev. B **86**, 174521 (2012).
35. E. Nicol and J. Carbotte, "Temperature dependence of the critical pair-breaking current in thin-film, strong-coupling superconductors," Phys. Rev. B **43**, 10210 (1991).
36. T. Kubo, "Superfluid flow in disordered superconductors with Dynes pair-breaking scattering: depairing current, kinetic inductance, and superheating field," Phys. Rev. Res. **2**, 033203 (2020).
37. A. Zotova and D. Y. Vodolazov, "Intrinsic detection efficiency of superconducting nanowire single photon detector in the modified hot spot model," Supercond. Sci. Technol. **27**, 125001 (2014).
38. J. J. Renema, Q. Wang, R. Gaudio, *et al.*, "Position-dependent local detection efficiency in a nanowire superconducting single-photon detector," Nano Lett. **15**, 4541–4545 (2015).
39. Q. Wang, J. J. Renema, A. Engel, *et al.*, "Local detection efficiency of a NbN superconducting single photon detector explored by a scattering scanning near-field optical microscope," Opt. Express **23**, 24873–24887 (2015).
40. Y.-Y. Hong, Y.-Z. Wang, W.-J. Zhang, *et al.*, "Impact of helium ion irradiation on the thermal properties of superconducting nanowire single-photon detectors," arXiv (2025).
41. Y. Wang, H. Li, L.-X. You, *et al.*, "Wavelength dependence of intrinsic detection efficiency of NbN superconducting nanowire single-photon detector," Chin. Phys. B **28**, 078502 (2019).

42. T. Yamashita, S. Miki, W. Qiu, *et al.*, "Temperature dependent performances of superconducting nanowire single-photon detectors in an ultralow-temperature region," Appl. Phys. Express **3**, 102502 (2010).
43. A. Kozorezov, C. Lambert, F. Marsili, *et al.*, "Fano fluctuations in superconducting-nanowire single-photon detectors," Phys. Rev. B **96**, 054507 (2017).
44. L. Embon, Y. Anahory, Ž.L. Jelić, *et al.*, "Imaging of super-fast dynamics and flow instabilities of superconducting vortices," Nat. Commun. **8**, 85 (2017).
45. R. Gaudio, Z. Zhou, D. Sahin, *et al.*, "Inhomogeneous critical current in nanowire superconducting single-photon detectors," Appl. Phys. Lett. **105**, 222602 (2014).
46. F. Marsili, V. B. Verma, J. A. Stern, *et al.*, "Detecting single infrared photons with 93% system efficiency," Nat. Photonics **7**, 210–214 (2013).
47. M. Ejrnaes, R. Cristiano, O. Quaranta, *et al.*, "A cascade switching superconducting single photon detector," Appl. Phys. Lett. **91**, 262509 (2007).
48. S. R. Patel, M. Colangelo, A. D. Beyer, *et al.*, "Improvements of readout signal integrity in mid-infrared superconducting nanowire single-photon detectors," Appl. Phys. Lett. **124**, 162604 (2024).
49. G. Gol'Tsman, K. Smirnov, P. Kouminov, *et al.*, "Fabrication of nanostructured superconducting single-photon detectors," IEEE Trans. Appl. Supercond. **13**, 192–195 (2003).
50. D. V. Reddy, N. Otrooshi, S. W. Nam, *et al.*, "Broadband polarization insensitivity and high detection efficiency in high-fill-factor superconducting microwire single-photon detectors," APL Photonics **7**, 051302 (2022).
51. D. Y. Vodolazov and F. Peeters, "Superconducting rectifier based on the asymmetric surface barrier effect," Phys. Rev. B **72**, 172508 (2005).
52. B. G. Oripov, D. S. Rampini, J. Allmaras, *et al.*, "A superconducting nanowire single-photon camera with 400,000 pixels," Nature **622**, 730–734 (2023).